

CoinFT: A Coin-Sized, Capacitive 6-Axis Force Torque Sensor for Robotic Applications

Hojung Choi^{*1}, Jun En Low^{*1}, Tae Myung Huh², Gabriela A. Uribe¹, Seongheon Hong¹,
Kenneth A. W. Hoffman¹, Julia Di¹, Tony G. Chen¹, Andrew A. Stanley³, and Mark R. Cutkosky¹

Abstract—We introduce CoinFT, a capacitive 6-axis force/torque (F/T) sensor that is compact, light, low-cost, and robust with an average mean-squared error of 0.11N for force and 0.84 mNm for moment when the input ranges from 0~10N and 0~4N in normal and shear directions, respectively. CoinFT is a stack of two rigid PCBs with comb-shaped electrodes connected by an array of silicone rubber pillars. The microcontroller interrogates the electrodes in different subsets in order to enhance sensitivity for measuring 6-axis F/T. The combination of desirable features of CoinFT enables various contact-rich robot interactions at a scale, across different embodiment domains including drones, robot end-effectors, and wearable haptic devices. We demonstrate the utility of CoinFT on drones by performing an attitude-based force control to perform tasks that require careful contact force modulation. The design, fabrication, and firmware of CoinFT are open-sourced at <https://hojung-choi.github.io/coinft.github.io/>.

I. INTRODUCTION

PRECISE force and torque measurement is vital for robots to perform contact-rich tasks safely and effectively. Tasks such as table wiping [1], assembly [2], or palpating soft tissue [3] require the application of force and torque within a specific range—sufficient to complete the task but not so excessive as to cause damage or waste energy. Depending on the application and interaction type, robots performing contact-rich tasks come in various forms, including robotic arms [4], grippers [5], drones [6], and wearable devices [7]. Therefore, equipping these diverse robotic platforms with sensors that can accurately measure force and torque is essential.

Extensive research has been dedicated to developing 6-axis force/torque (F/T) sensors using various transduction methods [8]. Commercially available sensors also exist, such as the Gamma (ATI Industries), and 6-axis F/T sensors from MinebeaMitsumi or ReSense. However, these sensors are challenging to adopt across different robotic platforms, particularly those requiring small, slim form factors and robustness. For example, while commercial sensors can be compact and lightweight, they are often too fragile to reliably withstand impacts from drone crashes or incidental contact on an end-effector. Their thickness also adds unnecessary bulk to haptic devices, making them cumbersome. Additionally, the cost of these sensors can be prohibitive, especially when attempting to sensorize multiple fingers of anthropomorphic robot hands such as the Leap hand [9]. Conversely, existing sensors that

are robust and more affordable tend to be bulky and heavy [10], limiting their applicability in compact platforms. For an effective and scalable integration across diverse robotic platforms interacting in unstructured environments, a sensor must be compact, lightweight, robust, and affordable.

In this paper, we introduce CoinFT, a capacitive 6-axis F/T sensor the size of a US quarter dollar, weighing 2g, with a material cost of less than \$10 (Fig. 1 (a)). CoinFT combines all the aforementioned desirable features of a 6-axis F/T sensor—compactness, lightweight, robustness, and affordability—unlocking various contact-rich robot interactions in unstructured environments. One particularly promising application for CoinFT is on drones performing forceful interactions with the environment. Drones have previously executed contact-rich tasks without force feedback [11] in controlled scenarios or through careful human teleoperation [6]. While force sensors have been demonstrated in such tasks, their bulkiness, weight, and fragility make them unsuitable for unstructured, outdoor environments [12]. CoinFT’s design addresses these challenges, making it a viable solution for drones operating in environments where large impulses from contact or crashes are common. Its lightweight nature minimally impacts drone operation time, and its compact size facilitates easy integration into even small drones. In this work, we demonstrate the use of CoinFT on a drone for contact modulation through PID force control and the deployment of objects onto environmental surfaces by applying a controlled range of force.

The contributions of this paper are as follows:

- The design, fabrication, and comprehensive characterization of CoinFT.
- Experimental validation of the feasibility of integrating CoinFT on drones by modulating contact force and deploying objects on environment surfaces.
- Open sourcing the design, fabrication, and firmware of CoinFT.

II. RELATED WORK

A. Multi-axial Force Torque Sensors

Given its critical role in various contact-rich tasks, significant research has focused on developing multi-axial F/T sensors using diverse transduction methods, including piezoresistive, capacitive, optical, magnetic, and pneumatic techniques [8]. Among these, piezoresistive approaches have been the most extensively explored, typically involving the attachment of multiple strain gauges to precisely machined structures,

¹Stanford University, CA, USA.

²University of California Santa Cruz, CA, USA.

³Reality Labs Research, Meta Platforms Inc, WA, USA.

commonly designed as cross-beam or parallel structures [8]. Piezoresistive sensing offers precise measurement capabilities with a high signal-to-noise ratio (SNR), facilitated by strain gauges and circuitry optimized for SNR amplification [13]. The availability of compact electronics and advanced machining techniques has also enabled the fabrication of compact sensors, which is why commercially available 6-axis F/T sensors predominantly utilize piezoresistive technology (MinebeaMitsumi and ReSense). However, despite these advantages, these sensors are often fragile and susceptible to impact, which can result in plastic deformation or even failure of the sensing medium [14].

Capacitive sensing is another widely adopted approach for designing 6-axis F/T sensors, valued for its potential to achieve a compact form factor while maintaining high sensitivity [8]. Compared to piezoresistive sensors, capacitive sensors can be relatively simpler to fabricate. Multiaxial F/T sensing via capacitive methods is typically achieved in one of two ways: using a single layer of sensing electrodes integrated with specially designed structures that deform and create distinct signal patterns upon input [15], [16], or employing multi-layer structures with electrodes, where each layer is more sensitive to specific subsets of forces and torques, generating unique signal patterns accordingly [17].

Optical sensing methods have been employed in the design of multi-axis F/T sensors by controlling the scattering or reflection of light within the system [18]. These methods can be broadly categorized into light intensity sensing [19], employing Fiber Bragg Grating (FBG) optical fibers [20], and vision-based [21] techniques. In traditional optical methods, variations in reflected light intensity at multiple locations are converted into measurements of force and torque [19]. FBG-based sensing leverages FBG fibers embedded in areas of higher strain within the sensor body, functioning similarly to strain gauges to precisely measure deformation [20]. Vision-based tactile sensing, on the other hand, involves using a compact camera to observe the deformation of a silicone rubber medium, often a robot fingertip, upon contact [21]. A recently popularized approach for force and torque sensing involves monitoring the deformation of specially patterned silicone rubber fingertips and employing data-driven models to infer the applied force and torque [21], [22]. Another method involves tracking the movement of a visual cue with a camera to deduce the load [23], [24]. Alternatively, gel deformation patterns can be remotely observed through an optical fiber, enabling the decoupling of the silicone gel from the sensing camera [25].

Other, less explored approaches in the design of multi-axial F/T sensors include piezoelectric [26], magnetic [27], [28], and pneumatic methods [10]. While piezoelectric effects have been utilized in these sensors, their susceptibility to charge leakage makes them less ideal for measuring static loads. Magnetic sensing techniques, which involve strategically positioning magnets and Hall effect sensors to detect forces and torques across six axes, have also been explored [27]. However, magnetic sensing is inherently vulnerable to external noise sources, such as the Earth's magnetic field or ferromagnetic objects. Additionally, similar design principles have

been applied in pneumatic sensors, where pressure differential patterns are created using an array of barometers [10].

B. Contact Based Interaction of Drones

Significant research has focused on enabling drones to avoid contact [29], and more recently, efforts have shifted toward allowing drones to interact with their environment through controlled and sustained contact, such as in perching [30] or performing tasks that require contact modulation [31]. Perching, in particular, has garnered attention for its ability to allow drones to remain in an environment without expending energy to stay aloft, thereby significantly increasing their operational time. To facilitate perching on horizontal [32] and vertical surfaces [33], bioinspired grippers [34] and control strategies [11] have been developed. While these approaches show promise for perching, they lack contact sensing, which limits the ability to assess perch stability or react to failures in real-time.

A number of research has explored the use of force-controlled contact with the environment through the integration of load cells [35]. These studies have investigated various applications, such as maintaining a consistent contact force while changing position using hybrid position-force controllers [36], analyzing surface textures by combining load cells with vision-based tactile sensors [12], and attaching objects to surfaces with custom-designed mechanisms [35]. However, the load cells used in these studies, typically commercial 6-axis F/T sensors, present challenges for real-world integration due to their high cost, fragility, and bulky readout electronics. In contrast, CoinFT, with its lightweight, compact design, robustness, and affordability, is ideally suited for drone applications.

III. COINFT

A. CoinFT Design

CoinFT is a capacitive 6-axis force/torque sensor. Its circular sensing area is 20 mm in diameter and approximately 2 mm in thickness (Fig. 1(c)), having a comparable form-factor to a quarter-dollar coin in the United States currency (Fig. 1(a)). With a total weight of 2 g, it consists of two 0.8 mm thick rigid PCBs (Printed Circuit Boards) connected by an array of 127 μ m thick cylindrical pillars cast from silicone rubber (TAP[®] Silicone RTV Mold-Making System). The radial density of pillars increases towards the edge of the PCB for improved strength against delamination. We employed a dense array of microns-wide pillars despite the added challenges in fabrication to retain sensitivity. Wider structures will increase effective stiffness of the pillar layer, which will be discussed in detail in Section III-D.

Each rigid PCB is multilayered, with four quadrants of a pair of comb-shaped electrodes on one side and a plane of electrode for passive shielding on the other side (Fig. 1(b), (c)). The upper sensing layer has eight physical electrodes while the lower sensing layer houses two physical electrodes (Fig. 1(b)). It is by leveraging this design with the unique capabilities of the microcontroller (Cypress, PSoC[™] 4100S) on CoinFT, that a pair of PCBs become sensitive to 6-axis F/T, which will be discussed in detail in Section III-B. The

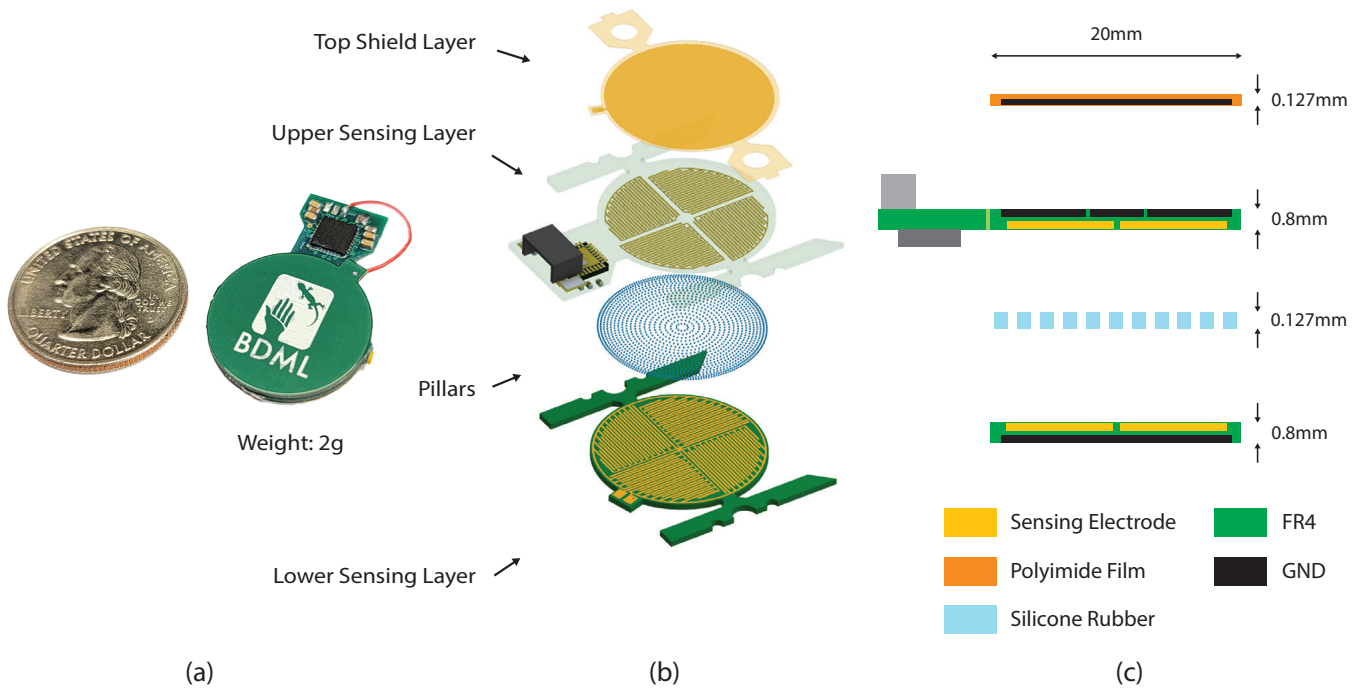


Fig. 1. (a) CoinFT is approximately the size of a U.S. quarter-dollar coin. (b) Exploded view of CoinFT. It consists of two rigid PCBs (upper and lower sensing layers) connected with an array of silicone rubber pillars. The fPCB top shield layer provides passive shielding. (c) Dimensions of each layer. The overall thickness is approximately 2 mm.

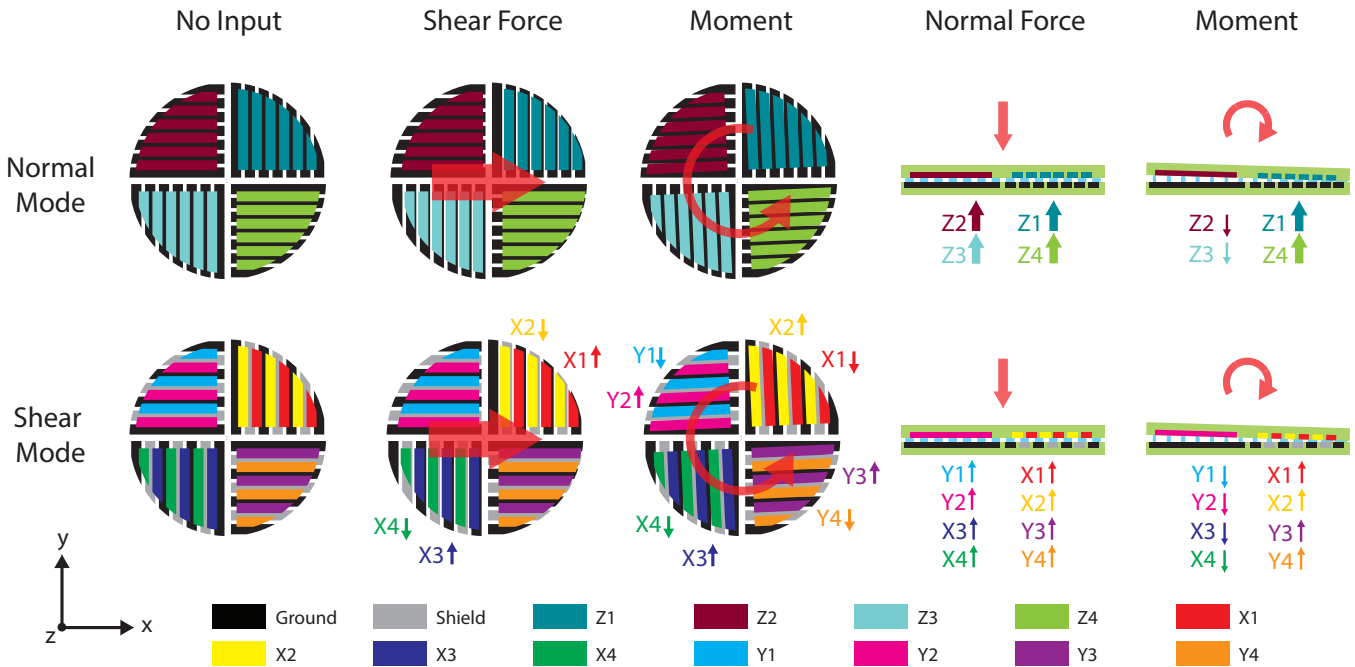


Fig. 2. CoinFT working principle. The microcontroller firmware is programmed to switch the pair of rigid PCBs between two different configurations - normal mode and shear mode. The capacitance signals collected from these two configurations produce a unique pattern under different force and torque inputs.

top shield layer made of a 127 μm thick fPCB (flexible Printed Circuit Board) is then added to provide additional passive shielding, as the via holes in the upper sensing layer can introduce noise from stray capacitance in the environment (Fig. 1 (b), (c)). Each PCB layer has structures for alignment on its sides, which is later removed during the final stages of

fabrication.

A tab (10 mm \times 11 mm) attached to the side of the circular sensing area houses the electronics necessary for capacitance sensing (Fig. 1 (b), (c)). A microcontroller with external capacitors measures and converts capacitance to digital counts using its native capacitance-to-digital conversion (CDC) module at 360 Hz. Signals can be acquired by other devices through

direct serial communication or USB ports through a serial to USB converter, such as a PSoC™ KitProg2, with a latency of 2 ms on average.

B. Working Principle

CoinFT measures 6-axis force and torque by observing the changes in capacitance signal patterns between the upper sensing layer and the lower sensing layer (Fig. 1). Capacitance is expressed as equation (1)

$$C = \frac{\varepsilon A}{d} \quad (1)$$

where C is capacitance, ε is the dielectric constant, A is the overlapping area of the electrodes, and d is the distance between the electrodes. The microcontroller firmware is programmed to switch the pair of rigid PCBs between two different electrode configurations every sampling sequence - normal mode and shear mode. This reconfiguration is achieved by modifying the internal electronic switches in the microcontroller, which either connect or disconnect the electrodes from the microcontroller's capacitance-to-digital conversion (CDC) module, a technique similar to that employed by Huh et al. [15].

In the normal mode, the pair of electrodes in each quadrant in the upper sensing layer are internally connected to function as a single electrode, effectively reducing the eight physical electrodes to four: $Z1$, $Z2$, $Z3$, and $Z4$ (Fig. 2). The two electrodes in the lower sensing layer are reconfigured to connect to *ground*. This design allows the normal mode to be sensitive to inputs that changes d , such as Fz , Mx , and My , but not to changes in A , which results from Fx , Fy , and Mz . Under Fz , all normal mode electrodes ($Z1$, $Z2$, $Z3$, and $Z4$) show a rise in signal, while under Mx or My , a differential pattern between pairs of normal mode electrodes is created (Fig. 2).

In the shear mode, each electrode in the upper sensing layer are kept as independent sensing electrodes ($X1$, $X2$, $X3$, $X4$, $Y1$, $Y2$, $Y3$, and $Y4$), while the electrodes in the lower sensing layer are configured such that the *ground* and *shield* electrodes form an alternating pattern (Fig. 2). The *shield* electrode actively mitigates interference from stray capacitance by being excited to the same electrical potential as the sensing electrodes, an innate capability of PSoC™ 4100S. This design allows the shear mode to be sensitive primarily to shear inputs such as Fx , Fy , and Tz . Under a shear pressure, the relative position of the upper sensing layer and the lower layer shifts laterally, changing A between a sensing electrode and *ground* electrode. Due to the negligible capacitance formation between a sensing electrode and a *shield* electrode, the relative position change results in a differential signal pattern in the shear mode. The comb shaped electrodes are populated in a way that allows the first and third quadrant of the shear mode is sensitive to loads in the X direction, while the second and fourth quadrants are sensitive to the Y direction. Under torsion (Tz), all four quadrants in the shear mode show a differential signal pattern. Unlike the normal mode configuration where there is negligible cross-modal sensitivity by design, there is

cross-coupling in the shear mode configuration. This effect and its implications will be discussed in detail Section III-D1. The unique signal pattern generated from the normal and shear mode configurations upon loads in different axes makes CoinFT, a pair of rigid PCBs, a 6-axis F/T sensor.

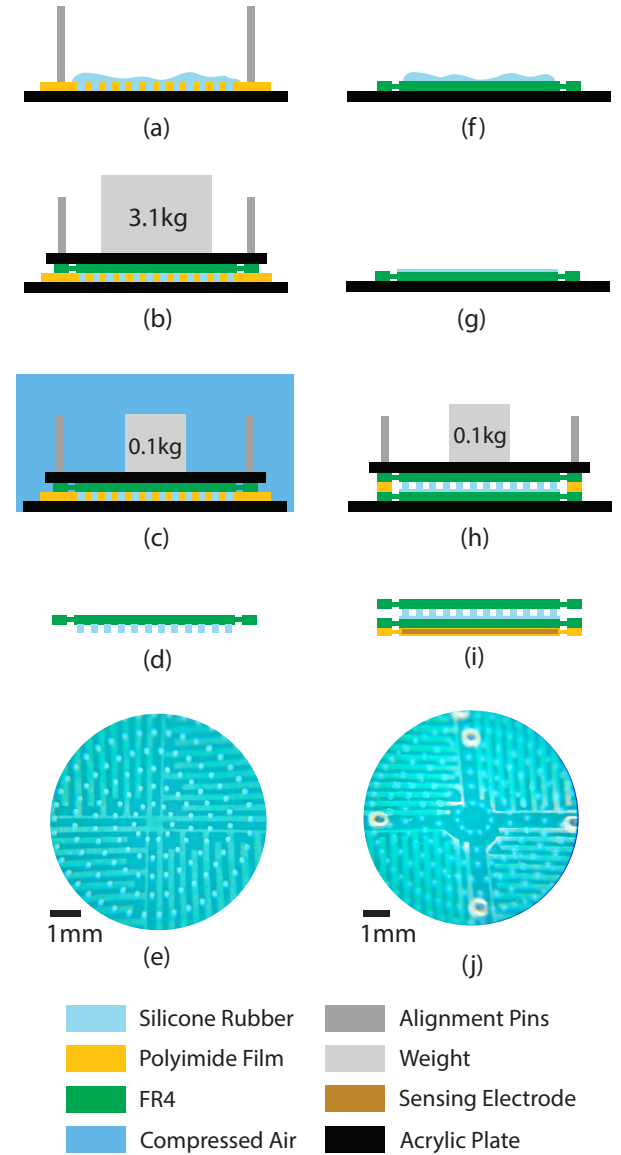


Fig. 3. The fabrication process of CoinFT. (a) Fresh uncured silicone is spread on a UV laser cut mask that is placed on an acrylic plate with alignment pins. (b) A primed lower sensing layer PCB and an acrylic plate for equal pressure distribution is stacked with a 3.1 kg weight. (c) With a 0.1 kg weight, the assembly is cured inside a pressurized chamber. (d),(e) Once the mask and acrylic plates are removed, the pillar layer is complete. (f) On a primed upper sensing layer PCB, fresh uncured silicone is spread. (g) The silicone layer is made thin and uniform through spin-coating. (h) The lower sensing layer with pillars is assembled with the upper sensing layer through precise distance control by adding spacers in between. A 0.1 kg weight and an acrylic plate for pressure distribution is added. (i) The top shield layer is attached using an adhesive. (j) The cross section of the pillar layer shows desirable bonding of the two PCB layers.

C. Sensor Fabrication

CoinFT is fabricated using the process illustrated in Fig. 3. A 127 μm polyimide film pillar mask cut by a UV laser cutter (DPSS Lasers Inc., Samurai UV Marking System) is placed on an acrylic plate using dowel pins for alignment. Vacuum degassed uncured silicone rubber (TAP[®] Silicone RTV Mold-Making System) is smeared on the surface of the mask to fill the cavities for pillars (Fig. 3 (a)). Then, the lower sensing layer PCB primed using DOWSIL[™] PR-1200 RTV Primer for enhanced adhesion is aligned and placed on the pillar mask. Another acrylic plate is placed on the assembly for equal pressure distribution and a 3.1 kg mass is added for 3 minutes to minimize the thickness of the base layer of the silicone pillars (Fig. 3 (b)). The 3 kg mass is removed, and the pillar assembly, with a 100 g mass added, is cast inside a pressure chamber for at least 12 hours at approximately 414 kPa to compress any remaining micro-bubbles inside the silicone rubber (Fig. 3 (c)). Once the acrylic plates and the pillar mask are removed, the pillar layer is complete (Fig. 3 (d), (e)).

On the upper sensing layer PCB, after the microcontroller and the electrical components are hand-soldered, the sensing area is primed and applied with vacuum degassed uncured silicone rubber (Fig. 3 (f)). Then, the silicone layer is spin-coated at 5000 rpm for 75 seconds to achieve a uniform and thin layer (Fig. 3 (g)). The pillar layer is attached to the upper sensing layer PCB with a 203 μm polyimide film spacer in between, to control the distance between the two PCBs. A 100 g mass and an acrylic plate is placed on top of the assembly to apply equally distributed pressure, ensuring that the pillars and the spun coat silicone layer are in contact (Fig. 3 (h)). The assembly is then cured inside a 65 $^{\circ}\text{C}$ oven for 72 hours. After the alignment pins and spacers are removed, the top shield layer fPCB is adhered to the other side of the upper sensing layer PCB using an adhesive (Henkel Corporation, Loctite 401 Instant Adhesive) (Fig. 3 (i)). The cross-section of the pillar assembly under a microscope is shown in Fig. 3 (j). The total cost of all components is less than \$10.

D. Sensor Characterization

A quantitative analysis using finite element analysis (FEA) and real sample testing has been conducted to understand the behavior of CoinFT. The FEA involved a structural analysis using ANSYS (Fig. 4 (h)) to investigate the deformation of the pillar array under different loading conditions, and an electrostatics analysis in COMSOL (Fig. 4 (i)), to study the change in capacitance in the sensing electrodes resulting from pillar deformation. The pillar mechanics was modelled using a linear elastic model with a high deformation option to account for the geometric nonlinearities. The Gent model [37] was applied to convert the shore hardness of the silicone rubber into Young's modulus. With the assumption that the silicone rubber is incompressible, the effective Young's modulus of each pillar was derived using a disk model of an elastomer bonded between two plates, as modeled by Haddow et al. [38], shown in (2).

$$E_e = E\left(1 + \frac{1}{2}\eta^{-2}\right) \quad (2)$$

E_e is the effective Young's modulus, E is the Young's modulus of the material, and η is the ratio between the height and radius of the pillars.

The dielectric constant of the silicone rubber was assumed to be 3.0, a common value for silicone rubber [39], while the dielectric constant of air was taken as 1.0. In order to verify the reliability of our FEA model, we compared the real and simulated response of CoinFT to normal force (Fig. 4 (d)), where the load for the real sample was given up to 10 N at 0.1 Hz. The FEA model closely matched the actual sample response, accurately capturing the stiffening effects due to pillar deformation at higher loads, and effectively representing the true behavior of CoinFT (Fig. 4 (d), (g)).

1) *CoinFT Calibration*: Based on the working principle from Fig. 2, CoinFT produces a distinguishable signal pattern from its 12 sensing electrodes (4 normal mode, 8 shear mode) under different force and torque loads. The simulated sensor response (Fig. 4 (a)-(c)) shows the distinguishable signal patterns under ideal alignment and distance of the upper and lower sensing layer PCBs. For sensor calibration, CoinFT is mounted on a commercial sensor (ATI Industrial Automation, Gamma) which provides ground truth force and torque information, while a combination of different loads are given from a human finger. A 2nd order least squares fit is used to map the raw capacitance signals into corresponding force and torque. The calibration results are shown in Fig. 5, and the mean square error (MSE) is provided in Table I. The minimum detectable force of CoinFT is 20 mN.

The 8 shear mode electrodes respond to inputs causing change in distance, F_z , M_x , and M_y , between the electrodes and the *ground* electrode (Fig. 4 (a)). While it is possible to calibrate the sensor using only the shear mode electrodes, the redundancy added by the high signal-to-noise ratio (SNR) by the normal mode signals (Fig. 4 (a)) significantly increase calibration accuracy, as shown in Table I. As expected, the increase in accuracy is more significant for F_z , M_x , and M_y .

2) *Sensitivity and Dynamic Range Tuning*: Different robotic applications require varying sensor dynamic range, sensitivity, and accuracy. For instance, fine control of a fingertip-mounted haptic device [40] requires high sensitivity to small forces within a dynamic range under 4 N in the

TABLE I
MEAN-SQUARED ERROR OF COINFT CALIBRATION RESULTS.

Input Range: 0~5 N Normal, 0~2 N Shear						
	Fx	Fy	Fz	Mx	My	Mz
Normal + Shear	0.04	0.04	0.05	0.32	0.31	0.24
Shear	0.04	0.04	0.11	0.34	0.32	0.24
Input Range: 0~10 N Normal, 0~4 N Shear						
	Fx	Fy	Fz	Mx	My	Mz
Normal + Shear	0.12	0.10	0.10	0.84	1.03	0.65
Shear	0.13	0.10	0.22	0.91	1.2	0.72

**"Normal + Shear" includes all 12 electrodes in the calibration process, while the "Shear" case uses only 8 electrodes from the shear mode. Forces are measured in N, and moments are in mNm. A CoinFT sample with a pillar diameter of 100 μm was used.

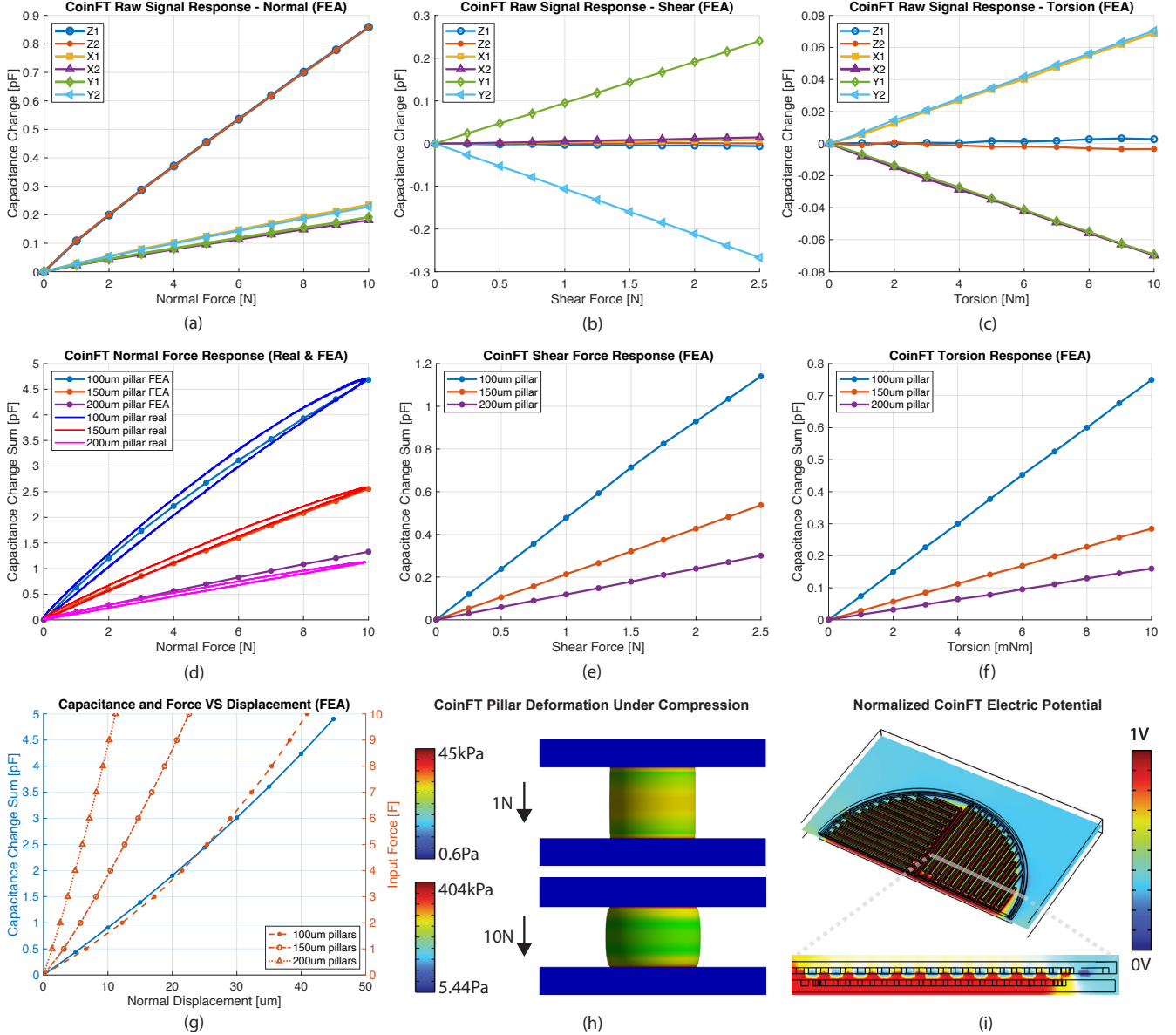


Fig. 4. CoinFT characterization using FEA. Raw capacitance response of a half of CoinFT (a) under normal force, (b) shear force, and (c) torsion. Full CoinFT response with varied pillar diameter under (d) normal force (real samples & FEA), (e) shear force (FEA), (f) and torsion (FEA). (g) Raw capacitance change with displacement and corresponding compressive force. (h) Structural modeling in FEA. (i) Electrostatics modeling in FEA.

normal direction, whereas measuring the ground reaction force of quadruped robot feet may require a range of up to 350 N [41], with less emphasis on sensitivity to small forces. The design of the pillar layer can be adjusted to alter its mechanical properties, meeting the specific requirements of different applications.

The effect of varying pillar diameter on sensor response is illustrated in Fig. 4(d)-(g). Both experimental and FEA results demonstrate a gradual decrease in sensitivity under normal load (Fig. 4(d), (g)). This reduction in sensitivity is attributed to the stiffening of the pillars as they compress. The lateral deformation of the pillars (Fig. 4(h)) increase their effective Young's modulus, as described in equation (2). Given that the sensitivity of the capacitance change to further

compression increases as shown in equation (1) and demonstrated in (Fig. 4(g)), we note that the stiffening effect is significant. For instance, the quadratic increase of stiffness and sensitivity of capacitance offset each other at lower displacements, resulting in an approximately linear capacitance–force relationship (Fig. 4(d), (g)). However, the stiffening effect outweighs the increase in capacitance change with higher deformation, explaining the decrease in sensitivity observed in Fig. 4(d).

The FEA results also illustrate that the sensitivity to changes in capacitance due to normal and shear forces, as well as torsion, is approximately inversely proportional to the cross-sectional area of the pillar array. Conversely, the dynamic range is proportional to the cross-sectional area of the pillar

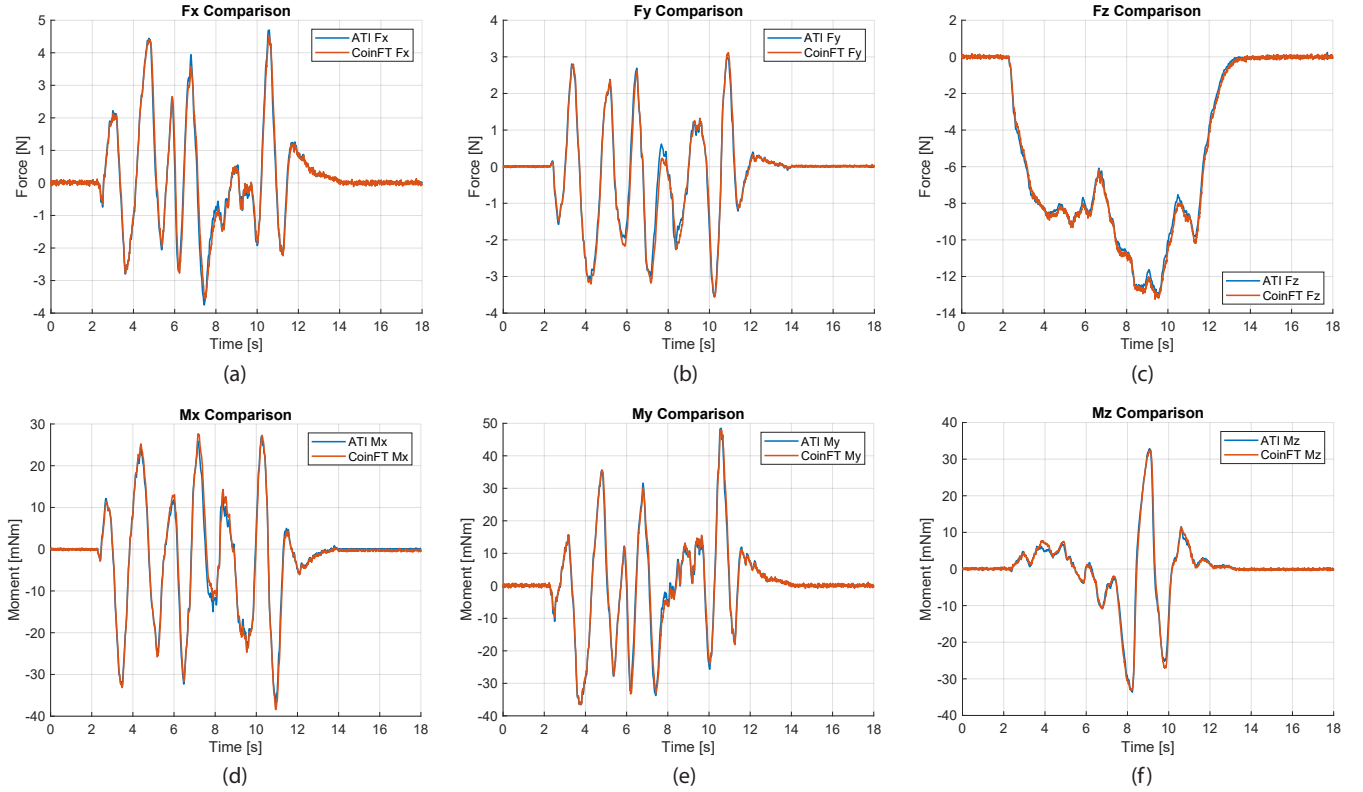


Fig. 5. Comparison of sensor readings between CoinFT and Gamma (ATI Industrial Automation) in (a) Fx, (b) Fy, (c) Fz, (d) Mx, (e) My, (f) Mz.

array.

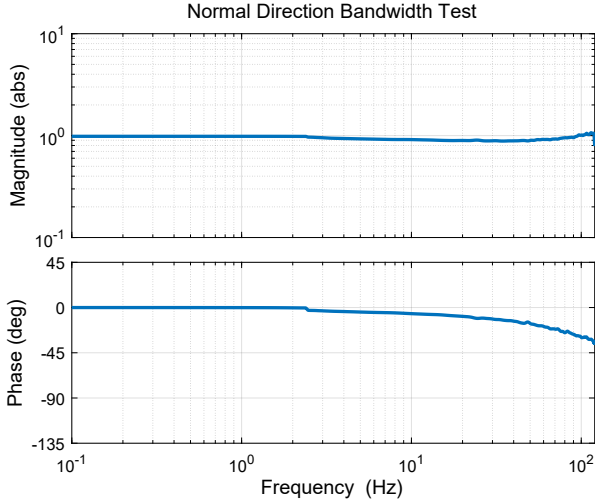
Additional mechanical parameters that can be adjusted in the pillar layer include the number of pillars, the material selection to alter the Young's modulus, and the arrangement pattern of the pillars. Notably, the torsional stiffness can be fine-tuned while maintaining consistent normal and shear stiffness by modifying the pillar pattern, as this alters the polar moment of inertia without affecting the overall cross-sectional area of the pillar layer. This capability is particularly valuable for applications such as wearable fingertip haptic devices that require high sensitivity of both forces and torque [40].

3) *Dynamic Response*: A frequency response analysis has been conducted to investigate the mechanical bandwidth of CoinFT (Fig. 6). A dual-mode muscle lever (Aurora Scientific Inc., 309C) has been used to provide a sinusoidal force sweep either in the normal or shear directions from 0 Hz \sim 120 Hz. The force input ranged from 0 N \sim 2 N in the normal direction and 0.1 N \sim 1.1 N in the shear direction. As shown in Fig. 6 (a), the magnitude response of CoinFT in the normal direction is kept above 70.7% (-3dB) of the input signal across the entire swept frequency. The phase lag is negligible up to 2.5 Hz, and gradually increases with higher frequency input where, at 120 Hz, the phase lag is -34.6° . The magnitude response in the shear direction (Fig. 6 (b)) starts to deteriorate at 2.45 Hz and reaches 70.7% (-3dB) of the input signal at 97 Hz. At that point, the phase delay is -94.2° . The cause of the phase lag is likely due to the innate hysteresis of silicone rubber material, as shown in Fig. 4 (d). These results show that the mechanical bandwidth of CoinFT is approximately 97 Hz.

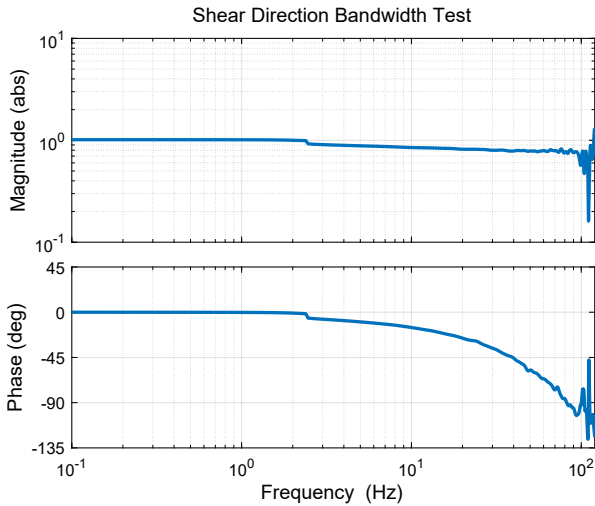
4) *Robustness*: Many robot applications involve incidental large impulses that can potentially damage commercially available 6-axis F/T sensors. Due to the compliance of the pillar arrays, CoinFT demonstrates reliable robustness against impacts. As shown in Fig. 7, CoinFT can accurately measure small loads of 1 N, 2 N, and 3 N even after sustaining an impact from a hammer that causes a force reading of 180 N. Such an impact would typically damage commercial sensors like the Gamma (ATI Industrial Automation) used for the CoinFT calibration. This level of robustness enables a broader range of robotic interactions beyond controlled environments, making the integration of 6-axis F/T sensors practical for real-world applications.

IV. CONTACT FORCE MODULATION OF AERIAL VEHICLES

Drones offer unique capabilities for performing contact-rich tasks in inaccessible areas, such as collecting plant samples from cliffs in Hawaii [6] or cleaning windows on tall buildings [42]. However, most drones lack contact sensing due to the fragility and cost of existing load cells. Integrating robust and affordable force sensing would greatly enhance drone utility. CoinFT addresses this challenge with its compact design, lightweight construction (6.7 g including the sensor and USB-to-serial bridge), and affordability (under \$10 per unit). CoinFT is also durable enough to withstand impacts common in real-world applications. In this section, we present a drone equipped with CoinFT and a force controller, enabling the drone to attach a package of electronics to a horizontal surface. This force-controlled interaction, unlocked by CoinFT,



(a)



(b)

Fig. 6. CoinFT frequency response in the (a) normal and (b) shear direction.

allows drones to perform tasks such as deploying sensor packages for environmental surveillance or conducting structural health monitoring on tall buildings. These sensor packages can continue to operate well beyond the limited flight time of the drones, providing valuable data to humans.

A. Drone with CoinFT

Our drone is a 127 mm frame quadrotor with an UpBoard companion computer and a PixRacer flight controller (Fig. 8). CoinFT is attached at the distal tip of a custom mount, which is connected in series with the proximal mount through a telescoping mechanism with rubber bands (Fig. 8(c)). The compliant element in series help reduce impact upon contact. CoinFT is connected to the UpBoard computer through a USB port. A socket is attached at the top of CoinFT which allows mounting different end-effectors for different tasks, such as a round tip for general contact or a package of electronics (Fig. 8(a) and (b)). The electronics package consists of an ESP32 microcontroller that uses four 12 V batteries in par-

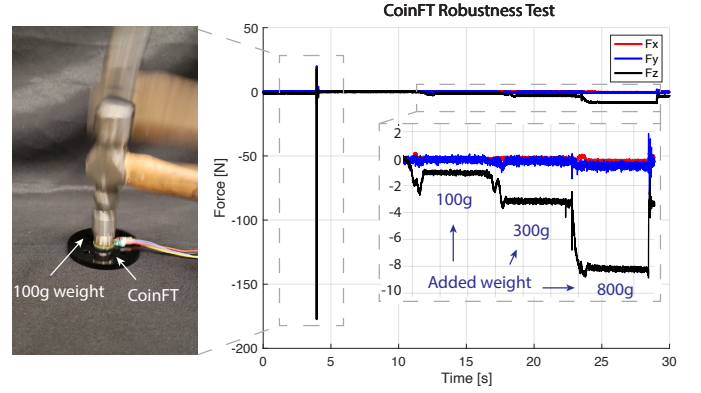


Fig. 7. CoinFT is robust. It can produce reliable force readings after being struck by a hammer.

allel to control a strip of LED to signal successful package deployment. Pressure sensitive adhesives are attached at the corners on the top side of the package. Since the package is not mechanically attached to the socket, the package will attach to a surface once sufficient pressure provides the necessary adhesion.

B. Attitude Controller for Contact

To simulate an unstructured environment, we designed a controller for the quadrotor that does not explicitly know the height of the contact surface, thus relying on CoinFT not only to execute force modulation but also to find the contact surface.

We assume the quadrotor has access to reliable full state information. While technologies exist to achieve this with on-board only sensors, implementing them falls outside the scope of this paper, so we utilize motion capture to assist state estimation by providing the drone with position information. We also provide the quadrotor with a minimum snap trajectory spline [43] that passes through the contact surface. This allows us to take a range of heights within which we are confident that the contact surface exists and transform it into a sequence of desired positions (\mathbf{p}_{des}), velocities (\mathbf{v}_{des}) and orientations (\mathbf{q}_{des}), for our controller to track while it searches for contact.

We interface with the PixRacer at the attitude control level, comprising of a commanded normalized thrust force (\hat{f}_{cmd}) and a commanded orientation (\mathbf{q}_{cmd}). We choose this level of control as it allows us to guarantee that the drone is stationary and perpendicular to the contact surface (through commanded orientation) and gives us direct control of the thrust for force modulation.

To account for the drone flight envelope including both in-contact and out-of-contact flight we use a switching, cascaded PID controller to advance from currently observed states $[\mathbf{p}_{obs} \ \mathbf{v}_{obs} \ \mathbf{q}_{obs}]$ to desired attitude commands \mathbf{u}_{cmd} . We start by taking the position and velocity error:

$$\mathbf{e}_p = \mathbf{p}_{obs} - \mathbf{p}_{des}, \quad \mathbf{e}_v = \mathbf{v}_{obs} - \mathbf{v}_{des}$$

From which we compute a desired force vector while accounting for gravity:

$$\mathbf{F}_{des} = -\mathbf{K}_p \mathbf{e}_p - \mathbf{K}_v \mathbf{e}_v - m\mathbf{g}$$

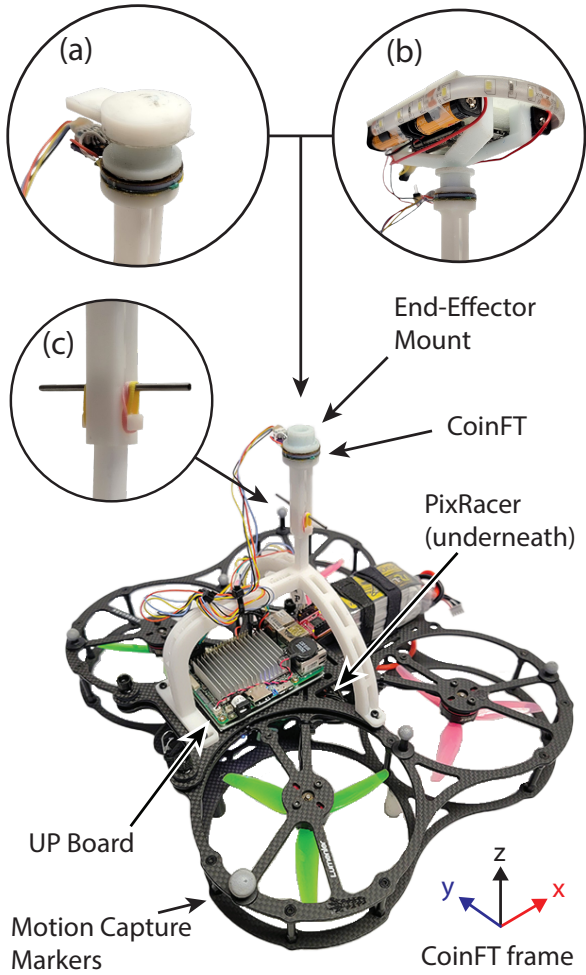


Fig. 8. Experimental setup for drones performing contact rich tasks. Different end-effectors can be attached to the CoinFT mount, such as (a) a tip for general contact or (b) a package of electronics to be attached on a surface. Compliance is added in series through a (C) telescoping mechanism with pre-tensioned rubber bands to mitigate impact upon contact.

where F_{des} is the desired force, m is the mass of the drone, g is the gravity vector, and (K_p, K_v) are positive definite gain matrices that switch between in-contact gains and out-of-contact gains:

$$K_p, K_v = \begin{cases} K_p^{oc}, K_v^{oc} & \text{if out of contact} \\ K_p^{ic}, K_v^{ic} & \text{if in contact} \end{cases}$$

Using the quaternion to rotation matrix to basis vector mapping $q_i \iff R_i \iff [x_i \ y_i \ z_i]$ on both the desired orientation (q_{des}) and commanded orientation (q_{cmd}), we can compute the latter by doing:

$$\begin{aligned} z_{cmd} &= \frac{F_{des}}{\|F_{des}\|} \\ y_{cmd} &= \frac{z_{cmd} \times x_{des}}{\|z_{cmd} \times x_{des}\|} \\ x_{cmd} &= y_{cmd} \times z_{des} \end{aligned}$$

To get the commanded normalized thrust force we start by getting a desired normalized thrust (f_{des}). This is done by invoking the quaternion to basis vector mapping to get z_{obs}

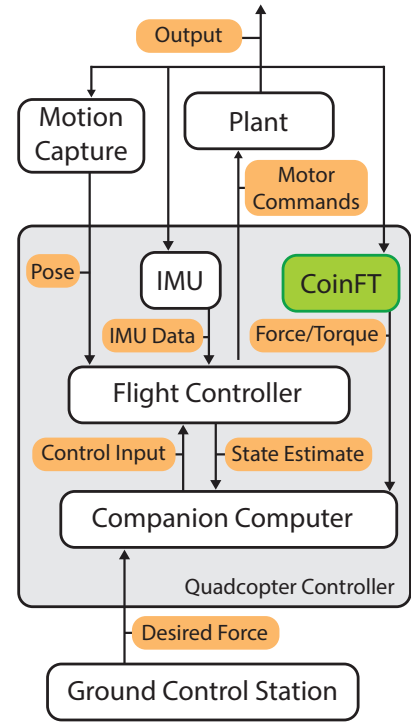


Fig. 9. System diagram of the integrated drone test setup.

from q_{obs} and then projecting the desired force vector onto it:

$$\begin{aligned} f_{des} &= F_{des} \cdot z_{obs} \\ \hat{f}_{des} &= k_f f_{des} \end{aligned}$$

where k_f is the thrust normalization coefficient. This is then fed into a state machine (Algorithm 1) for thrust control that switches modes during contact events and tracks desired contact forces using CoinFT feedback. The two key features of the state machine is a linear search function for the contact force and a PID tracking controller. The former enables graceful transitions when the initial desired contact force is large while the latter not only enables us to hold but also track a changing desired contact force. Combined, these allow for more consistent and safer performance. Given an observed force on CoinFT (f_{oc}), desired force on CoinFT (f_{dc}) and current time (t_{cr}) we perform the following to get the commanded normalized thrust. Assuming compressive force, we use the absolute values of the CoinFT reading in the normal direction (Algorithm 1).

The CoinFT feedback data lets us use the state machine to dynamically switch the gain matrices K_p, K_v where we use the out of contact gains when in FREE mode and in contact gains otherwise.

C. Force Controlled Deployment of Objects on Environment Surfaces

To test the designed force controller and perform electronics package delivery tasks, we conducted flight tests. The test setup includes a laser-cut acrylic plate horizontally attached to a structure made of extruded aluminum frames (Fig. 10 (a)),

Algorithm 1 Thrust State Machine and PID Controller

```

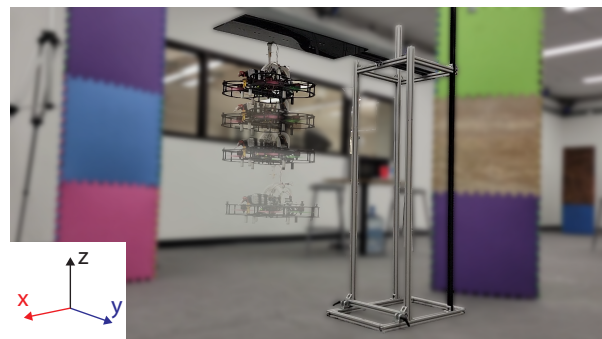
1: Inputs:  $\hat{f}_{des}$ ,  $f_{oc}$ ,  $f_{dc}$ ,  $t_{cr}$ 
2: Outputs:  $\hat{f}_{cmd}$ ,  $S$ 
3: Parameters: Force Increment  $\Delta f$ , Proportional Gain  $k_p$ ,
   Integral Gain  $k_i$ , Derivative Gain  $k_d$ , Hold Duration  $T$ 
4: Initialization:
5:  $e_{prev} \leftarrow 0$ ,  $\int e dt \leftarrow 0$ ,  $\hat{f}_{cmd} \leftarrow \hat{f}_{des}$ ,  $S \leftarrow \text{FREE}$ 
6: if  $S$  is FREE then
7:    $\hat{f}_{cmd} \leftarrow \hat{f}_{des}$ 
8:   if  $f_{oc} > 0$  then
9:      $S \leftarrow \text{SEARCH}$ 
10: else if  $S$  is SEARCH then
11:    $\hat{f}_{cmd} \leftarrow \hat{f}_{cmd} + \Delta f$ 
12:   if  $f_{oc} \geq f_{dc}$  then
13:      $f_{hold} \leftarrow \hat{f}_{cmd}$ ,  $t_{prev} \leftarrow t_{cr}$ ,  $t_0 \leftarrow t_{cr}$ 
14:      $S \leftarrow \text{HOLD}$ 
15: else if  $S$  is HOLD then
16:    $\Delta t \leftarrow t_{cr} - t_{prev}$ ,  $e_{curr} \leftarrow f_{oc} - f_{dc}$ 
17:    $P \leftarrow k_p e_{curr}$ ,  $I \leftarrow I + k_i e_{curr} \Delta t$ ,  $D \leftarrow k_d \frac{e_{curr} - e_{prev}}{\Delta t}$ 
18:    $\hat{f}_{cmd} \leftarrow f_{hold} + P + I + D$ 
19:    $e_{prev} \leftarrow e_{curr}$ 
20:   if  $t_{cr} - t_0 \geq T$  then
21:     break

```

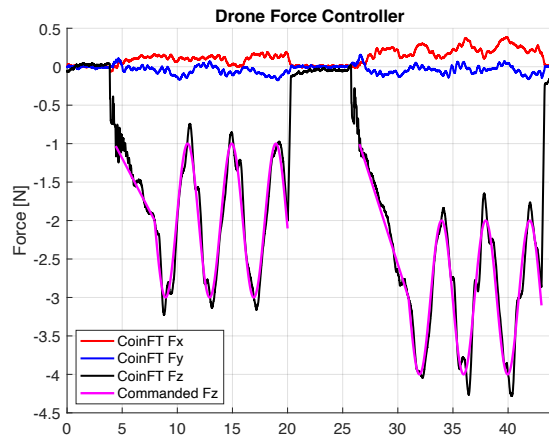
simulating arbitrary environmental surfaces. The integrated system consists of a ground control station (PC), motion capture system (OptiTrack, NaturalPoint, Inc.), and a drone equipped with a companion computer, flight controller, IMU, and a CoinFT sensor (Fig. 9). The proposed attitude controller runs on the companion computer, providing control inputs to the flight controller, which then converts these inputs into PWM signals for the four motors.

The performance of the proposed attitude-based force controller is illustrated in Fig. 10(b). A hemispherical contact tip (Fig. 8 (a)) is mounted on the drone. During the *SEARCH* state, the motor thrust ramps linearly until the drone senses contact. Contact is signaled by normal force reaching a desired value, which is initially set by the ground control station. Upon contact, the controller transitions to the *HOLD* state, where it tracks a pre-programmed sinusoidal force command. The force controller demonstrates accurate tracking, with an RMS error of 0.1779 N.

Using the force controller, the drone can attach electronics packages to environmental surfaces such as a tree branch by applying a precise range of force—sufficient to complete the task but not so excessive as to damage the environment, or expend more energy than required. The electronics package, equipped with pressure-sensitive adhesives and weighing 95 g (Fig. 8 (b)), is mounted on the drone. Adequate pressure must be applied for the package to adhere securely to a surface. The drone initially hovers below the horizontal surface and ascends until contact is detected. Upon contact, the contact force ramps up to a commanded value of 0.7 N, which registers as approximately 1.7 N in CoinFT due to the package’s weight (Fig. 11 (a)). The drone breaks contact and descends while still sensing approximately 1 N in CoinFT, detecting that the



(a)



(b)

Fig. 10. Results of the force controller test. (a) The drone ascends until contact is made with the test setup, where it initiates force control. (b) CoinFT readings and commanded normal force.

package has not adhered properly (Fig. 11 (b)). The drone then autonomously increases the desired contact force to 5 N (Fig. 11 (c)). After applying the higher force, the drone no longer senses the package’s weight through CoinFT and sends an *ON* command to the electronics package via WiFi, activating the LEDs to signal task success (Fig. 11 (d)). These precisely controlled interactions are valuable for attaching objects, such as sensor packages, to potentially fragile surfaces like tree branches or for performing general force-controlled tasks, such as cleaning windows on tall buildings.

V. DISCUSSION & FUTURE WORK

While this paper focuses primarily on demonstrating CoinFT’s capabilities on drone platforms, the sensor’s versatility extends to a wide range of other robotic applications. CoinFT has already been used in wearable haptic devices, where it measures and controls the contact force between the device and the human subject. For instance, Sarac et al. [44] used CoinFT to reveal that people perceive different intensities when the same force is applied in normal versus shear directions. Yoshida et al. [7] employed CoinFT to ensure consistency in user studies by initializing the haptic device tactor based on contact force rather than position. This approach is crucial for accommodating variations in users’ body shapes, as position-based initialization does not consistently deliver uniform haptic feedback. CoinFT’s slim and compact design

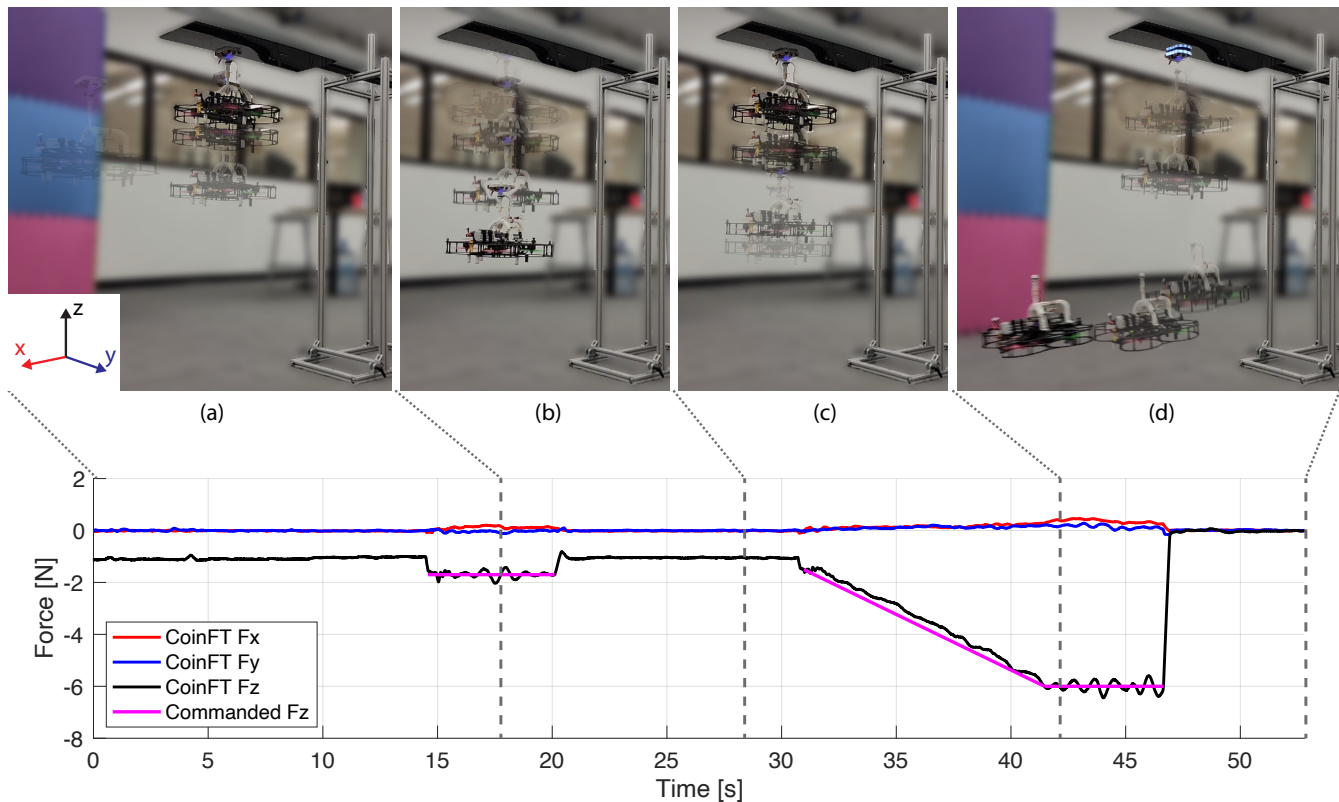


Fig. 11. Drone attaching a package of electronics on environment surfaces using force control. (a) The drone gently presses the package on the horizontal surface. (b) After descending, it still feels the weight of the package through CoinFT. (c) The drone presses the package with a larger force on the surface. (d) Upon descent, it no longer feels the weight of the package. It turns on the package and leaves the scene.

also makes it highly suitable for wearable fingertip devices [40].

CoinFT has also been directly attached under the fingertips of a commercial anthropomorphic robot hand [45] for learning force-informed actions from kinesthetic demonstrations. In such setup, it can sense contact force for controlled, forceful interaction or track the contact point by utilizing force and torque information for intrinsic tactile sensing [46]. When connected via I2C communication, multiple CoinFTs can be integrated to sensorize all fingers, enhancing the robot hand’s ability to perform fine-manipulation tasks. Its low cost and robustness against incidental impacts make CoinFT particularly desirable for robot hands operating in unstructured and cluttered environments.

While the current form factor of CoinFT has been designed to showcase its versatility across various robotic platforms such as drones, robot fingertips, and haptic devices, it can be tailored to meet the specific needs of other applications. For example, CoinFT can be made even narrower to sensorize compact medical devices [47]. The tradeoff in this case would be a decrease in sensitivity due to the reduced sensing area. Conversely, CoinFT could be scaled up to fit the form factor of quadruped or humanoid feet, allowing for the measurement of ground reaction forces (GRF). The larger sensing area in this configuration would enable both higher sensitivity and an expanded dynamic range. This would require a careful selection of design parameters to meet the specifications on

sensitivity and dynamic range, as discussed in Section III-D.

While CoinFT is versatile and suitable for a wide range of robotic applications, it is not intended as a direct replacement for existing commercial sensors like the Gamma (ATI Industrial Automation). The mechanical bandwidth of CoinFT is an order of magnitude lower than that of the Gamma (1 kHz), making it less capable of detecting highly dynamic contacts. Additionally, the Gamma offers a finer force resolution even with its high dynamic response capabilities. Although CoinFT is highly robust against large compressive impulses, it is less resilient to large tensile impacts, as the bonding between the silicone rubber pillars and the PCB may fail under such conditions.

Other challenges must be considered when using CoinFT. While shielding has been implemented to prevent the coupling of stray capacitance, the surface-mounted electrodes of the chip remain partially exposed, which can result in imperfect shielding. Furthermore, the silicone rubber pillars may creep under long-term sustained loads, altering the mechanical characteristics of the pillar array and necessitating re-calibration. The current thin PCB might not be entirely rigid and could deform out of plane under significant local pressure, potentially reducing calibration accuracy. This issue, however, can be mitigated by using a slightly thicker PCB or bonding a thin layer of stiff material. Additionally, variations in ambient temperature may cause slight deformations in the sensing electrodes or the internal electronics of the chip, leading to drift

in the capacitance signal. Despite these limitations, CoinFT remains valuable for many robotic applications where such high precision and bandwidth in a 6-axis F/T sensor is not essential, and where robustness and low cost are prioritized.

The proposed attitude control strategy is expected to be effective only in the directions where the drone is fully actuated. Through experimentation, we have observed that precise force control in the lateral direction is challenging with a quadrotor due to the coupling between tilt and lateral displacement. However, CoinFT and the proposed controller can be valuable for modulating lateral contact force when using a fully actuated drone [12], [36].

VI. CONCLUSION

In this paper, we introduced CoinFT, a coin-sized capacitive 6-axis F/T sensor composed of a pair of specially designed PCBs connected by an array of silicone rubber pillars. Through a comprehensive characterization, CoinFT has demonstrated a unique combination of compactness, robustness, affordability, and reliable performance. These qualities make it an ideal solution for various robotic applications, including drones, robot hands, and wearable haptic devices, particularly in real-world scenarios where large incidental impulses are common.

While CoinFT offers considerable versatility, it is not intended as a replacement for commercially available 6-axis F/T sensors, which typically offer a larger dynamic range, finer force resolution, and higher bandwidth. Instead, CoinFT excels in applications where such high-end specifications are not a priority, while low cost and scalable deployment are desirable.

We demonstrated the utility of CoinFT by integrating it with a drone to perform force-controlled tasks, such as attaching an electronics package to environmental surfaces. This capability is an example of CoinFT's potential to democratize the use of 6-axis F/T sensors across a broad range of robotic platforms, enabling more widespread adoption in applications that demand robustness and cost-effectiveness without sacrificing essential functionality.

ACKNOWLEDGEMENTS

This work was supported in part by Meta Reality Labs Research and the Kwanjeong Fellowship. The authors thank Claire Chen, Kyle Yoshida, Crystal Winston, Mine Sarac, and Alice Wu for exciting and insightful discussions about CoinFT applications.

REFERENCES

- [1] H. T. Suh, N. Kuppaswamy, T. Pang, P. Mitiguy, A. Alspach, and R. Tedrake, "Seed: Series elastic end effectors in 6d for visuotactile tool use," in *IEEE/RSJ International Conference on Intelligent Robots and Systems*, 2022, pp. 4684–4691.
- [2] R. Song, F. Li, W. Quan, X. Yang, and J. Zhao, "Skill learning for robotic assembly based on visual perspectives and force sensing," *Robotics and Autonomous Systems*, vol. 135, p. 103651, 2021.
- [3] J. Konstantinova, G. Cotugno, P. Dasgupta, K. Althoefer, and T. Nanayakkara, "Autonomous robotic palpation of soft tissue using the modulation of applied force," in *IEEE International Conference on Biomedical Robotics and Biomechanics*, 2016.
- [4] P. M. Grice, M. D. Killpack, A. Jain, S. Vaish, J. Hawke, and C. C. Kemp, "Whole-arm tactile sensing for beneficial and acceptable contact during robotic assistance," in *2013 IEEE 13th International Conference on Rehabilitation Robotics*, 2013, pp. 1–8.
- [5] M. A. Lin, R. Thomasson, G. Uribe, H. Choi, and M. R. Cutkosky, "Exploratory hand: Leveraging safe contact to facilitate manipulation in cluttered spaces," *IEEE Robotics and Automation Letters*, vol. 6, no. 3, pp. 5159–5166, 2021.
- [6] H. La Vigne, G. Charron, J. Rachiele-Tremblay, D. Rancourt, B. Nyberg, and A. Lussier Desbiens, "Collecting critically endangered cliff plants using a drone-based sampling manipulator," *Scientific Reports*, vol. 12, no. 1, 2022.
- [7] K. T. Yoshida, Z. A. Zook, H. Choi, M. Luo, M. K. O'Malley, and A. M. Okamura, "Design and evaluation of a 3-dof haptic device for directional shear cues on the forearm," *IEEE Transactions on Haptics*, pp. 1–13, 2024.
- [8] M. Y. Cao, S. Laws, and F. R. y. Baena, "Six-axis force/torque sensors for robotics applications: A review," *IEEE Sensors Journal*, vol. 21, no. 24, pp. 27 238–27 251, 2021.
- [9] K. Shaw, A. Agarwal, and D. Pathak, "Leap hand: Low-cost, efficient, and anthropomorphic hand for robot learning," 2023. [Online]. Available: <https://arxiv.org/abs/2309.06440>
- [10] J. W. Guggenheim, L. P. Jentoft, Y. Tenzer, and R. D. Howe, "Robust and inexpensive six-axis force-torque sensors using mems barometers," *IEEE/ASME Transactions on Mechatronics*, vol. 22, no. 2, pp. 838–844, 2017.
- [11] T. G. Chen, K. A. W. Hoffmann, J. E. Low, K. Nagami, D. Lentink, and M. R. Cutkosky, "Aerial grasping and the velocity sufficiency region," *IEEE Robotics and Automation Letters*, vol. 7, no. 4, pp. 10 009–10 016, 2022.
- [12] X. Guo, G. He, M. Mousaei, J. Geng, G. Shi, and S. Scherer, "Aerial interaction with tactile sensing," 2023. [Online]. Available: <https://arxiv.org/abs/2310.00142>
- [13] S. S. Kumar and B. D. Pant, "Design principles and considerations for the 'ideal' silicon piezoresistive pressure sensor: a focused review," *Microsystem Technologies*, vol. 20, no. 7, p. 1213–1247, 2014.
- [14] S. Stassi, V. Cauda, G. Canavese, and C. Pirri, "Flexible tactile sensing based on piezoresistive composites: A review," *Sensors*, vol. 14, no. 3, p. 5296–5332, 2014.
- [15] T. M. Huh, H. Choi, S. Willcox, S. Moon, and M. R. Cutkosky, "Dynamically reconfigurable tactile sensor for robotic manipulation," *IEEE Robotics and Automation Letters*, vol. 5, no. 2, pp. 2562–2569, 2020.
- [16] U. Kim, H. Jeong, H. Do, J. Park, and C. Park, "Six-axis force/torque fingertip sensor for an anthropomorphic robot hand," *IEEE Robotics and Automation Letters*, vol. 5, no. 4, pp. 5566–5572, 2020.
- [17] X. A. Wu, S. A. Suresh, H. Jiang, J. V. Ulmen, E. W. Hawkes, D. L. Christensen, and M. R. Cutkosky, "Tactile sensing for gecko-inspired adhesion," in *IEEE/RSJ International Conference on Intelligent Robots and Systems*, 2015, pp. 1501–1507.
- [18] N. Yao and S. Wang, "Recent progress of optical tactile sensors: A review," *Optics & Laser Technology*, vol. 176, p. 111040, 2024.
- [19] O. Al-Mai, M. Ahmadi, and J. Albert, "Design, development and calibration of a lightweight, compliant six-axis optical force/torque sensor," *IEEE Sensors Journal*, vol. 18, no. 17, pp. 7005–7014, 2018.
- [20] L. Xiong, Y. Guo, G. Jiang, X. Zhou, L. Jiang, and H. Liu, "Six-dimensional force/torque sensor based on fiber bragg gratings with low coupling," *IEEE Transactions on Industrial Electronics*, vol. 68, no. 5, pp. 4079–4089, 2021.
- [21] W. K. Do, B. Jurewicz, and M. Kennedy, "Densetact 2.0: Optical tactile sensor for shape and force reconstruction," in *IEEE International Conference on Robotics and Automation*, 2023, pp. 12 549–12 555.

- [22] W. Yuan, S. Dong, and E. Adelson, "Gelsight: High-resolution robot tactile sensors for estimating geometry and force," *Sensors*, vol. 17, no. 12, p. 2762, 2017.
- [23] W. Li, M. Wang, J. Li, Y. Su, D. K. Jha, X. Qian, K. Althoefer, and H. Liu, "L³ f-touch: A wireless gelsight with decoupled tactile and three-axis force sensing," *IEEE Robotics and Automation Letters*, vol. 8, no. 8, pp. 5148–5155, 2023.
- [24] W. Li, A. Alomainy, I. Vitanov, Y. Noh, P. Qi, and K. Althoefer, "F-touch sensor: Concurrent geometry perception and multi-axis force measurement," *IEEE Sensors Journal*, vol. 21, no. 4, pp. 4300–4309, 2021.
- [25] D. Baimukashev, Z. Kappassov, and H. A. Varol, "Shear, torsion and pressure tactile sensor via plastic optofiber guided imaging," *IEEE Robotics and Automation Letters*, vol. 5, no. 2, pp. 2618–2625, 2020.
- [26] Y.-j. Li, X.-s. Xu, G.-c. Wang, S.-k. Cao, N.-j. Chen, and X. Sun, "Fault-tolerant measurement mechanism research on pre-tightened four-point supported piezoelectric six-dimensional force/torque sensor," *Mechanical Systems and Signal Processing*, vol. 135, p. 106420, 2020.
- [27] D. G. Black, A. Hossein Hadi Hosseinabadi, N. Rangga Pradnyawira, M. Nogami, and S. E. Salcudean, "Low-profile 6-axis differential magnetic force/torque sensing," *IEEE Transactions on Medical Robotics and Bionics*, vol. 6, no. 3, pp. 992–1003, 2024.
- [28] H. Choi, D. Brouwer, M. A. Lin, K. T. Yoshida, C. Rognon, B. Stephens-Fripp, A. M. Okamura, and M. R. Cutkosky, "Deep learning classification of touch gestures using distributed normal and shear force," *International Conference on Intelligent Robots and Systems*, pp. 3659–3665, 2022.
- [29] M. R. Rezaee, N. A. W. A. Hamid, M. Hussin, and Z. A. Zukarnain, "Comprehensive review of drones collision avoidance schemes: Challenges and open issues," *IEEE Transactions on Intelligent Transportation Systems*, vol. 25, no. 7, pp. 6397–6426, 2024.
- [30] J. Meng, J. Buzzatto, Y. Liu, and M. Liarokapis, "On aerial robots with grasping and perching capabilities: A comprehensive review," *Frontiers in Robotics and AI*, vol. 8, 2022.
- [31] E. Aucone, S. Kirchgeorg, A. Valentini, L. Pellissier, K. Deiner, and S. Mintchev, "Drone-assisted collection of environmental dna from tree branches for biodiversity monitoring," *Science Robotics*, vol. 8, no. 74, 2023.
- [32] A. Firouzeh, J. Lee, H. Yang, D. Lee, and K.-J. Cho, "Perching and grasping using a passive dynamic bioinspired gripper," *IEEE Transactions on Robotics*, vol. 40, pp. 213–225, 2024.
- [33] D. Mehanovic, D. Rancourt, and A. L. Desbiens, "Fast and efficient aerial climbing of vertical surfaces using fixed-wing uavs," *IEEE Robotics and Automation Letters*, vol. 4, no. 1, pp. 97–104, 2019.
- [34] W. R. T. Roderick, M. R. Cutkosky, and D. Lentink, "Bird-inspired dynamic grasping and perching in arboreal environments," *Science Robotics*, vol. 6, no. 61, 2021.
- [35] P. Spieler, S. X. Wei, M. Li, A. Galassi, K. Uckert, A. Kalantari, and J. W. Burdick, "Parsec: An aerial platform for autonomous deployment of self-anchoring payloads on natural vertical surfaces," in *2023 IEEE International Conference on Robotics and Automation (ICRA)*, 2023, pp. 5331–5337.
- [36] K. Bodie, M. Brunner, M. Pantic, S. Walser, P. Pfändler, U. Angst, R. Siegwart, and J. Nieto, "Active interaction force control for contact-based inspection with a fully actuated aerial vehicle," *IEEE Transactions on Robotics*, vol. 37, no. 3, pp. 709–722, 2021.
- [37] A. N. Gent, "On the relation between indentation hardness and young's modulus," *Rubber Chemistry and Technology*, vol. 31, no. 4, pp. 896–906, 1958.
- [38] J. Haddow and R. Ogden, "Compression of bonded elastic bodies," *Journal of the Mechanics and Physics of Solids*, vol. 36, no. 5, p. 551–579, 1988.
- [39] E. Cho, L. L. Y. Chiu, M. Lee, D. Naila, S. Sadanand, S. D. Waldman, and D. Sussman, "Characterization of mechanical and dielectric properties of silicone rubber," *Polymers*, vol. 13, no. 11, p. 1831, Jun. 2021.
- [40] S. R. Williams, J. M. Suchoski, Z. Chua, and A. M. Okamura, "A 4-degree-of-freedom parallel origami haptic device for normal, shear, and torsion feedback," *IEEE Robotics and Automation Letters*, vol. 7, no. 2, pp. 3310–3317, 2022.
- [41] M. Y. Chuah and S. Kim, "Enabling force sensing during ground locomotion: A bio-inspired, multi-axis, composite force sensor using discrete pressure mapping," *IEEE Sensors Journal*, vol. 14, no. 5, pp. 1693–1703, 2014.
- [42] A. A. Hulaibi, H. Wahid, S. A. Saif, J. Sadeq, S. Esmaili, and M. Kandil, "Skybot - a novel autonomous window cleaning drone," in *International Conference on Electrical, Communication and Computer Engineering*, 2023, pp. 1–6.
- [43] D. Mellinger and V. Kumar, "Minimum snap trajectory generation and control for quadrotors," in *2011 IEEE international conference on robotics and automation*. IEEE, 2011, pp. 2520–2525.
- [44] M. Sarac, T. M. Huh, H. Choi, M. R. Cutkosky, M. D. Luca, and A. M. Okamura, "Perceived intensities of normal and shear skin stimuli using a wearable haptic bracelet," *IEEE Robotics and Automation Letters*, vol. 7, no. 3, pp. 6099–6106, 2022.
- [45] C. Chen, Z. Yu, H. Choi, M. Cutkosky, and J. Bohg, "Dexforce: Extracting force-informed actions from kinesthetic demonstrations for dexterous manipulation," 2025. [Online]. Available: <https://arxiv.org/abs/2501.10356>
- [46] M. R. Cutkosky and W. Provancher, *Force and Tactile Sensing*. Springer International Publishing, 2016, p. 717–736.
- [47] Z. Chua and A. M. Okamura, "A modular 3-degrees-of-freedom force sensor for robot-assisted minimally invasive surgery research," *Sensors*, vol. 23, no. 11, p. 5230, May 2023.